Chapter 5

Synthesis, characterization, and hetero-photocatalytic studies of $Bi_4SrTi_4O_{15}$ ceramic

5.1 Introduction

Efficient Solar energy harvesting to produce green hydrogen through water splitting and degradation of organic pollutants is one of the critical aspects which needs urgent development. Transition metal based oxide for the above purposes has been extensively used under UV light irradiation, however, catalysts active under visible light conditions are relatively rare. Rhodamine B is a type of xanthene dye that is extensively used in the textile industry as a coloring agent. Natural degradation of Rhodamine B in anaerobic conditions produces harmful and carcinogenic chemicals like aromatic amines. Therefore, other ways of elimination, such as photochemical degradation of Rhodamine B from industrial wastewater, are the demand of the time (Naresh and Mandal 2014; Viswanathan 2018).

A large number of reports using metal oxides in bulk or in nanostructure form have been introduced for photocatalytic applications. Perovskites are a class of oxide known to exist in two- and three-dimensional structures. Notably, Bi has been used in a majority of the perovskite based photocatalysts that are active in visible region. Introduction of Bi in Perovskite structure provides a few major advantages such as (I) It shifts the absorption adage to the visible region by Bi 6s and O 2p hybridization, (II) Increased mobility of holes on dispersed band facilitate photo-oxidation (Benedek et al. 2015).

Among the photocatalytic activity of the Bi^{3+} containing materials in visible light, the Aurivillius phases are notable. The Bismuth Layered Perovskite Aurivillius phases are layered perovskites where the layered structure $(A_{m-1}B_mO_{3m+1})^{2-}$ exists in alternating layers of perovskite slabs, and the fluorite-like structure of $(Bi_2O_2)^{2+}$ units. Where m represents m-octahedra thick

perovskite where A denotes large 12 co-ordinate cation (K^+, Na^+, Pb^{2+}, Ca^{2+}, Ba^{2+}, Sr^{2+}, Bi^{3+}) and rare earth elements, B represents small 6 co-ordinate cation (Ti^{4+}, Nb^{5+}, Ta^{5+}, Mo^{6+}, W^{6+}, etc.),. Study of single layer (m = 1) Aurivillius type perovskite oxides such as Bi_2MoO_6 and Bi_2WO_6 (Shang et al. 2011; Zhang et al. 2011 May) in photocatalytic activities have been extensively done. In recent times, the four-layer (m = 4) Aurivillius phase, $Bi_4XTi_4O_{15}$ (where X is any large above-mentioned cations occupying A site in the perovskite), has sought much attention for its photocatalytic and ferroelectric properties (Hervoches et al. 2002). The layered structure of this Aurivillius oxide, besides providing an improved charge separation, also exhibits enhanced probability for the not only separation but also for the diffusion of photogenerated electrons-holes pairs when compared to the non-layered photocatalysts (Liu et al. 2014; Rana et al. 2006; Sunkara and Misra 2008; Venkatasubramanian et al. 2008). The reason for this separation and diffusion is the occurrence of lattice sites of reduction and oxidation in an isolated fashion on the surface and edges of the ultrathin units of layers sheets. In a layered crystalline structure, the photogenerated holes diffuse through the sub-nanometer length and reach to the surface of the sheet. On the surface of the sheet, the holes are trapped by the water molecules, which allows the electrons to effectively reach the sheet edges, enhancing the charge separation(Liu et al. 2010). These features of layered Aurivillius oxides make them efficient photocatalysts whose efficiency can be improved by the addition of metal, acting as a reservoir of the photogenerated electrons (Misra et al. 2012; Liang et al. 2017).

Besides, Aurivillius oxides has a peculiar crystalline structure allowing polarization possible in two directions, i.e., along the a-axis and c-axis, resulting in anisotropy. These polarization vectors switch directions, thus enabling these materials to possess a high dielectric

constant (Galasso and Kestigan 2007). Photocatalytic activity of $Bi_4XTi_4O_{15}$ towards organic pollutants degradation by visible-light irradiation such as isopropyl alcohol, RhB and acetaldehyde is already reported with not-so satisfactory results

Thus, in the present work, we explored a member of Aurivillius oxide $Bi_4SrTi_4O_{15}$ (BSTO), synthesized by the chemical route and studied its photocatalytic activity in the degradation of Rhodamine B dye. Due to its unique crystal structure, BSTO exhibits high dielectric constant, peculiar electrical properties and enhanced light harvesting properties with the prolonged lifetime of carriers facilitating improved catalytic performance and higher thermal and chemical stability.

5.2 Experimental Section

$Bi_4SrTi_4O_{15}$ (BSTO) ceramic was synthesized employing chemical route synthesis. Starting materials used were strontium nitrate $Sr(NO_3)_2$ (99% Merck, India), $Bi(NO_3)_3.5H_2O$ (99% Merck, India), Titanium oxide (oxide TiO2 99% Merck, India) and for complexating fuel citric acid (Citric acid $C_6H_8O_7$,99.5%, Emparta, India) is taken. The Sr^{+2}, Bi^{+3} ions in their stoichiometric amount of salt and TiO_2 in stoichiometric amount of Ti^{4+} along with citric acid, equivalent to metal ions, were dissolved in distilled water to form the reaction mixture. This reaction mixture was heated at 70–80 °C on a hot plate for approximately 24 to 48 hours with continuous stirring. After the water was completely evaporated, the fluffy mass left, burnt with sooty flame. Finally, we obtained dry ash, which was crushed to fine powder employing agate and mortar. This fine powder was calcined at 950 °C. The PVA binder was then added to calcined powder to transform cylindrical pellets by adding on applying 5 tons of pressure for 50-60 seconds. The pellet of specific diameter and thickness was sintered at 950 °C for 8 h and then used for characterization and measurements.

5.2.1 Photocatalytic Experiment

The BSTO ceramic was tested for its application in hetero-photocatalytic activity in dye degradation. Aerobic degradation of Rhodamine B dye in solar light was examined using the material synthesized. The hetero-photocatalytic test was conducted using 0.6 mg BSTO and 3 ml aqueous solution of Rhodamine B dye (dye concentration 8.38 mg/L) in a quartz cuvette of the path length of 1cm. The reaction mixture was continuously stirred for 60 min in the dark preceding solar irradiation to attain adsorption equilibrium. Then, the reaction mixture was exposed to irradiation by solar light. The hetero-photocatalytic efficiency of BSTO was evaluated by recording the UV-Vis absorption spectra at 554 nm (RhB) at a fixed time interval.

In order to detect the active species generated due to photo-irradiation on the material during the experiment, 0.5 mM of some chemical scavengers were added in separate reaction mixtures and tested. Scavengers used were potassium iodide (KI) for holes (h^+), parabenzoquinone (PBQ) for superoxide radicals ($O2^{\bullet-}$) and isopropyl alcohol (IPA) for hydroxyl radicals ($^{\bullet}OH$).

5.3 Characterization

The diffraction pattern of sintered $Bi_4SrTi_4O_{15}$ (BSTO) ceramic was recorded by X-ray diffractometer (XRD, Rigaku miniflex 600, Japan) using Cu-Kα radiation (λ = 1.54 Å) with 2°/min scan rate. The Fourier Transform Infrared (FTIR) spectra were characterized using KBr pellets by ATR FTIR (Bruker, ALPHA model) Spectrophotometer in the frequency range 500–1500 cm^{-1}. The UV-visible (UV-Vis) spectrum of sintered powder was examined by a UV-Vis spectrophotometer (UV2600, Shimadzu). The surface morphology of ceramic pellet was observed by scanning electron microscope (ZEISS model, EVO18 Germany), whereas its elemental compositions were analyzed by Energy dispersive X-ray (EDX) spectroscopy (Oxford instrument;

USA). For determination of particle shape and size Transmission electron microscope (TEM, FEI TECANI G2 20 TWIN; USA) was employed. The zeta potential of the material was measured by a dynamic light scattering technique using a Zetasizer Nano-ZS (Malvern Instruments, Malvern, UK). The Brunauer–Emmett–Teller (BET) surface area was examined by nitrogen adsorption-desorption isotherm measurements at 77.350K on a Quantachrome NOVA2000E device. The pore size distribution plot was attained by the Barret–Joyner–Halenda (BJH) model. X-ray photoelectron spectra (XPS) was recorded using PHI 5000 Versaprobe II photoelectron spectrometer (ULVAC-PHI) using Al Kα X-ray beam. Magnetic measurements were accomplished with a Quantum Design MPMS-3, at applied a magnetic field of ±2 T over a temperature range 5–300 K. Additionally, temperature dependent field cooling (FC) and Zero field cooling (ZFC) magnetization were recorded at 100 Oe applied field using SQUID VSM dc magnetometer at the same range of temperature.

5.4 Results and Discussion

High-resolution x-ray diffraction (HR-XRD) patterns of BSTO ceramic sintered at 850 °C for 8 h is displayed in figure 5.1. The diffraction pattern obtained in HR-XRD spectra correctly matches with JCPDS card no (43-0973) and all the peaks were indexed referring to it. Thus, the single-phase formation of pure BSTO ceramic is validated.

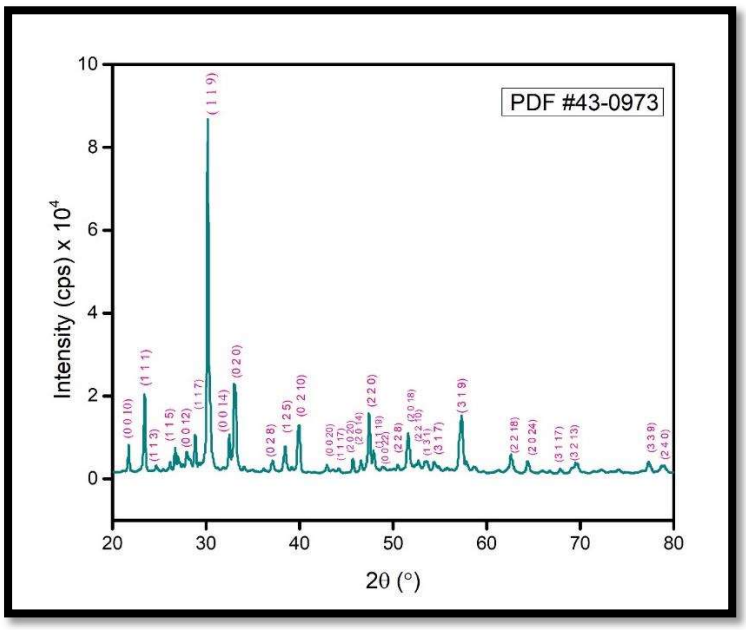

Figure 5.1 HR-XRD patterns of BSTO ceramic sintered at 950 °C for 8 h.

The crystal structure for BSTO ceramic was found to be an orthorhombic structure. The average crystallite size of BSTO ceramic is found to be 38.53 nm, which was obtained by taking the mean of six intense XRD peaks of the ceramic using the Debye-Scherrer formula.

$$D = \frac{k\lambda}{\beta \cos\theta} \tag{5.1}$$

where k is the crystal shape coefficient taken as 0.99. λ is the wavelength (1.54 Å) of the X-ray used, θ is Bragg's diffraction angle, and β (in radians) represents peak width of the diffraction peak at half-maxima (FWHM), respectively(Drits 1997).

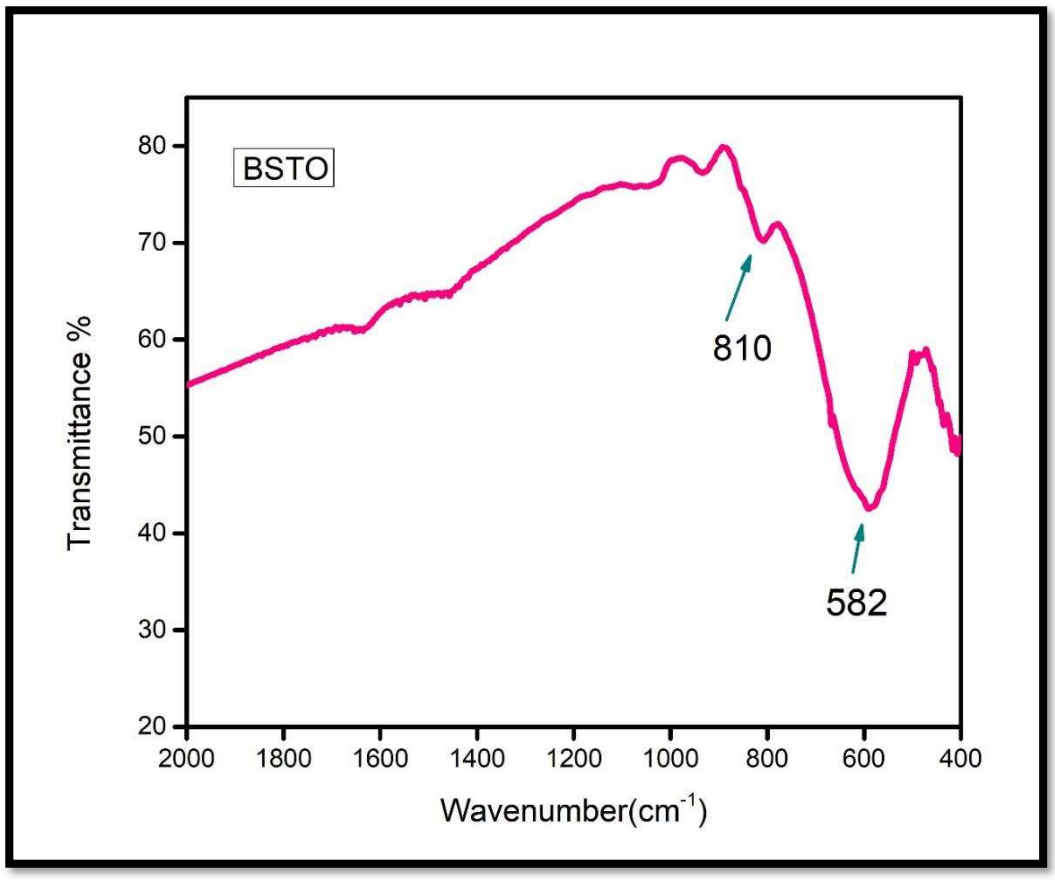

Figure 5.2 FT-IR spectra BSTO ceramic

FTIR spectra for BSTO ceramic is available in figure 5.2, recorded in the fingerprint range of 500–1500 cm^{-1} frequency. Only bands that appear are due to metal-oxides bonds of the metals present in the ceramic. The peak at 582 cm^{-1} is associated with Ti-O bond vibration(Sun et al. 2007; Kumar et al. 2018), and another peak at 810 cm^{-1} is observed due to the stretching vibration of Bi–O bond(Hou et al. 2011). It indicates towards purity of the ceramic.

Figure 5.3 (a) depicts Selected area diffraction (SAED) pattern of the polycrystalline BSTO ceramic with distinct bright spot patterns matching to planes (1 1 9), (1 1 7), (0 0 12), (0 0 6) and (1 1 1). Bright field TEM image of the BSTO is illustrated in figure 5.3 (b). It validates the

orthorhombic structure of the material as discussed in HR-XRD assessment. The mean particle size for BSTO ceramic was measured to be 114 ±2 nm..High-resolution TEM images can be seen in figure 5.3 (c). The value of inter-planer spacing d was obtained to be 3.87 Å for the corresponding planes of BSTO ceramic (Giannuzzi and Stevie 1999).

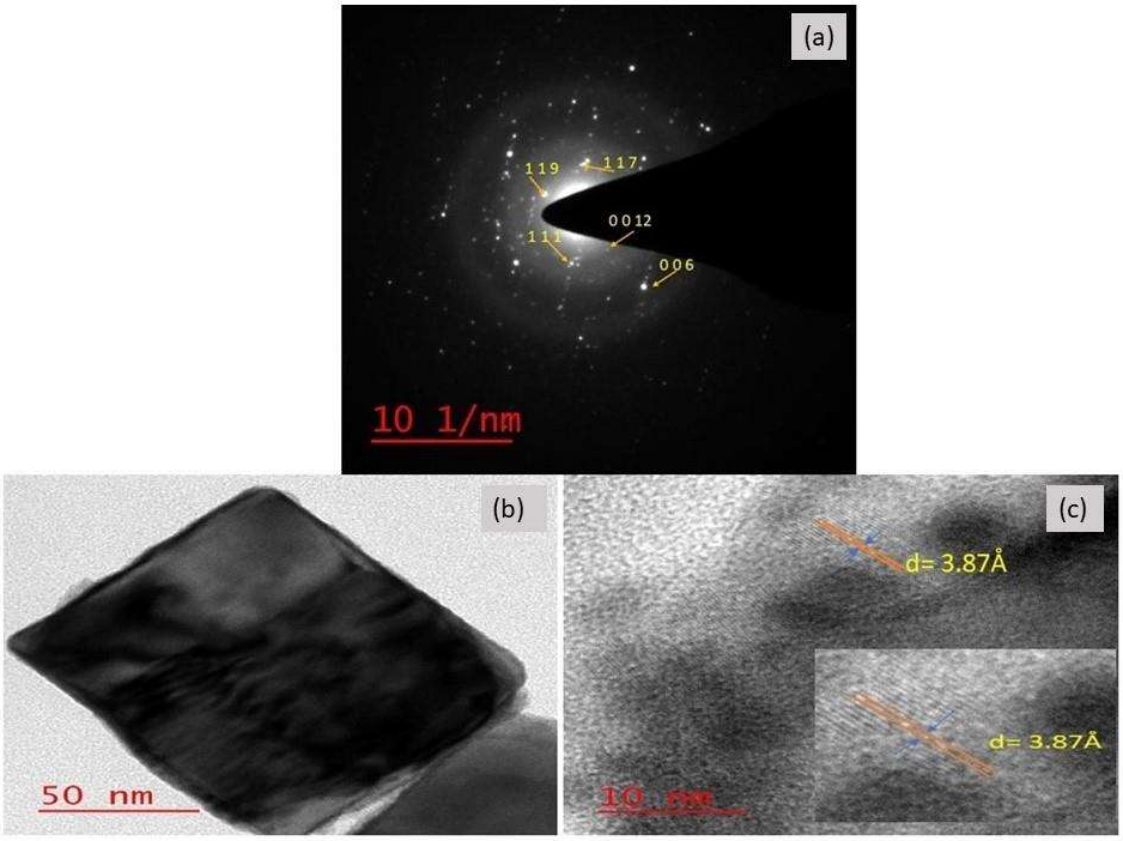

Figure 5.3 (a) SAED patterns (b) Bright Field TEM Images of BSTO ceramic and (c). HR-TEM images showing d-spacing.

SEM images in figure 5.4 illustrate the surface morphology of BSTO ceramic. It clearly indicates bimodal grain distribution The surface morphology observed on the gold-coated surface is depicted in figure 5.4 (a), reveals the presence of pellet-like grains separated by grain boundaries (Mohammed and Abdullah). The average grain size of BSTO is calculated using ImageJ software and found to be 447.27 nm. SEM analysis witnesses a larger average grain size than that of

crystallite size obtained from XRD measurement as the former is formed by aggregation of the latter. Figure 5.4 (b) illustrates the EDX spectrum for BSTO ceramic, which reveals the presence of Ba, Bi, Ti, and O elements in BSTO ceramic, which confirms the purity of materials.

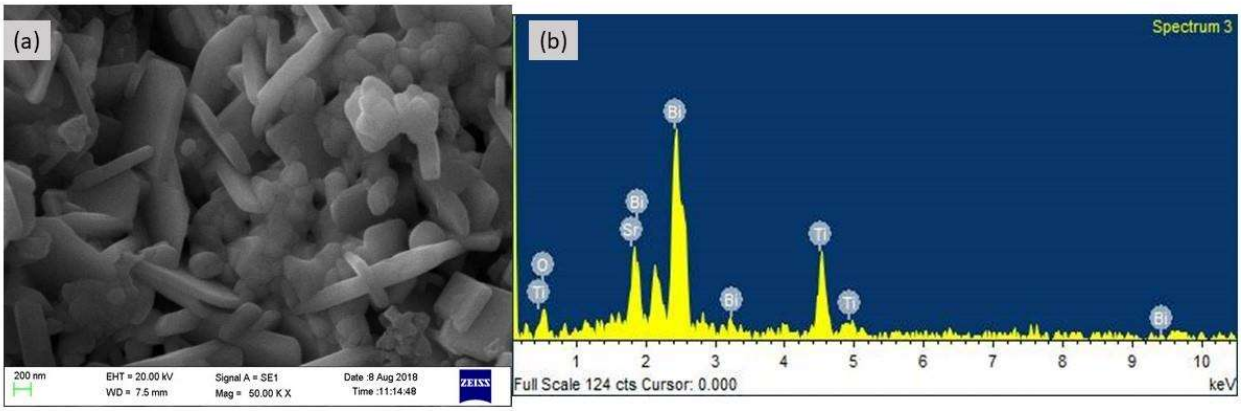

Figure 5.4 (a) SEM micrograph and (b) EDX spectra of BSTO ceramic.

AFM analysis of BSTO ceramic was done using tapping mode as depicted in figure 5.5. The histogram of grain size of particles is shown in figure 5.5 (a), indicating that most of the grains are in size range of 0.6-0.8 um in BSTO ceramic, which is in accordance with SEM and TEM results. The distributions of particles on the surface are illustrated by a 3-dimensional AFM image on the scanned area of 20 µm x 20 µm in figure 5.5 (b). Comparable grain size with clear grain boundaries is observed in 2-dimensional AFM images for BSTO ceramic is explained in figure 5.5 (c). The observed value of average roughness (Ra), root mean square roughness (Rq), maximum profile peak height and maximum profile valley depth for the 3-dimensional image of BSTO ceramic are mentioned in table 5.1.

Table 5.1 Data of AFM analysis of BSTO ceramic sintered at 950 °C for 8 h.

Average roughness (Ra)	36.116 nm
Root Mean Square roughness (Rq)	46.161 nm
Maximum Profile Peak Height	145.521 nm
Maximum Profile Valley Depth	108.791 nm

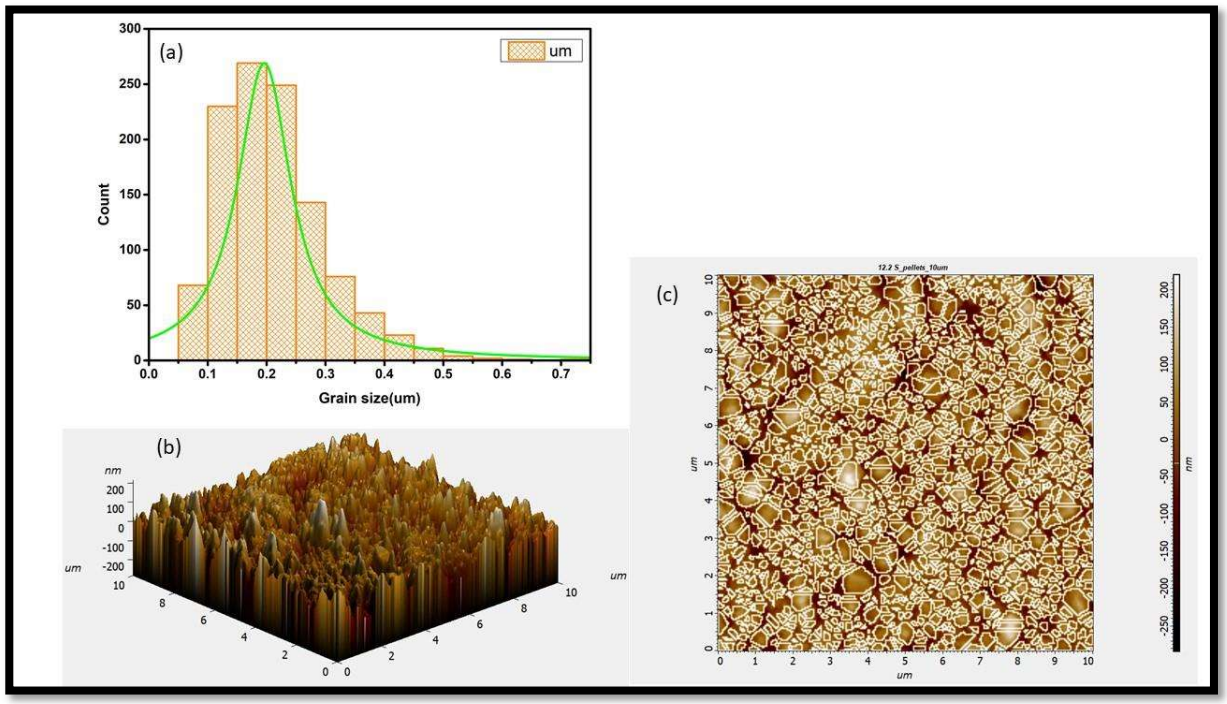

Figure 5.5 (a) Histogram graph for the particle size distribution, (b) 3-D for surface roughness and (c) 2-D watershed images for grain boundary of BSTO ceramic.

The zeta potential of the material was determined by a Zetasizer Nano-ZS employing the dynamic light scattering technique shown in figure 5.6 (a). The zeta potential of a particle is characteristic particle property as it is decisive for the stability of the particle in suspension form in the solution phase(Hoo et al. 2008). A distinct zeta potential value, either positive or negative, theoretically

informs the stabilization of particles in suspension(Shukla et al. 2013 Apr). As a consequence of like electric charges on particles, electrostatic repulsion exists among them, thus preventing them from coagulation and precipitation (Feng and Huang 2001). The zeta potential of BSTO was obtained to be −28.3 mV. This high negative value confirms the existence of the stable particle suspension, which facilitates its photocatalytic activity in dye degradation. Zetasizer Nano-ZS employing dynamic light scattering technique is also helpful in determining the particle size of the material. It can be witnessed from figure 5.6 (b) that the mean particle size is 41.87 nm [PDI] = 0.34)

(X-ray photoelectron spectroscopic (XPS) analysis was led to attaining the knowledge of the oxidation state of the elements composing the BSTO ceramic along with the electronic environment around them (Bantawal and Krishna Bhat 2018). The correction for the binding energies of the specimen surface charge acquired through the XPS analysis, reference was set to the C1s peak at 285.6eV (Singh et al. 2020). The high-resolution X-ray photoelectron spectroscopic (HRXPS) spectrum of the BSTO ceramic is depicted in figure 5.7 (a)–(d). The presence of elements such as bismuth, titanium, oxygen, and strontium in the material was verified. In figure 5.7 (a) high-resolution XPS spectrum of Ti 2p has been deconvoluted, resulting in three peaks. Among the three, the first two peaks are characteristic of Ti(IV), while the third one is caused due to Bi 4d. The peaks at 457.5 eV and 463.5 eV are characteristic of Ti $2p_{3/2}$ and Ti $2p_{1/2}$ binding energies, respectively. Another peak at 465.9 eV is characteristic of the binding energies of Bi $4d_{3/2}$. In the vicinity of 465.5 eV, a broad hump is observed, formed due to the partially overlapped peaks of Ti 2p1/2 and Bi 4d3/2 (Chu et al. 2002; Hou et al. 2013). Figure 5.7 (b) illustrates the High-resolution XPS spectra of bismuth confirming the presence of Bi^{+3}. Two

distinct peaks are obtained on deconvolution of the spectra. The peaks at 159.1 eV and 165.5 eV are characteristics of the binding energies of Bi $4f_{5/2}$ and Bi $4f_{7/2}$, respectively,(Hou et al. 2013; Zhao et al. 2019). Another peak seen at 162.5 eV may be assigned to Bismuth metal (Bi^0) (Li et al. 2017).

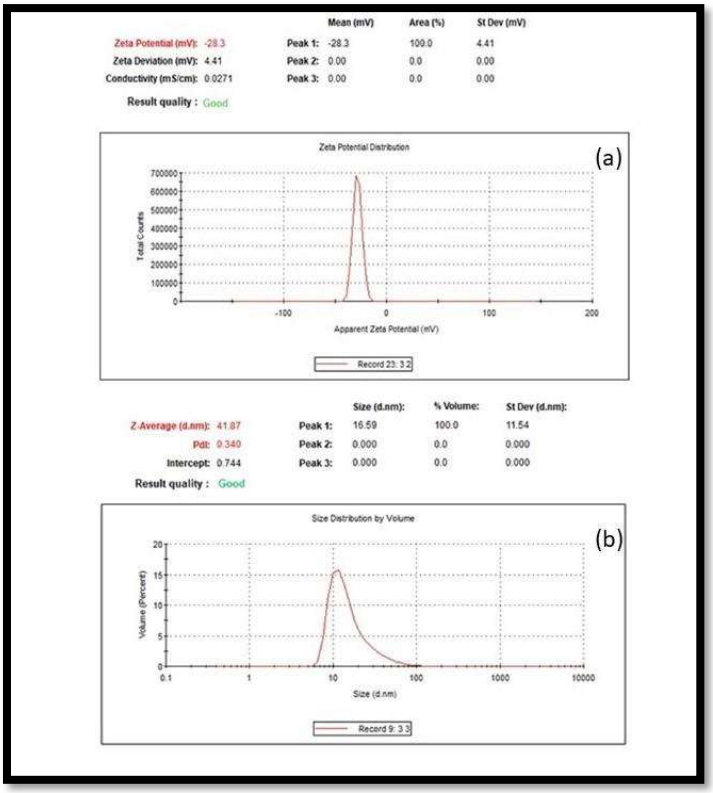

Figure 5.6 Zeta potential distribution(a) and particle size distribution(b) of BSTO ceramic.

Figure 5.7(c) depicts High-resolution XPS spectra of oxygen, revealing a widely asymmetric spectrum of O 1s, postulating the existence of all sorts of chemical states of O present in the material. The deconvolution of asymmetric broad O1s spectrum results in two main components: lattice oxygen species ($O_{lattice}$) at 529.8 eV binding energy and surface adsorbed oxygen ($O_{adsorbed}$) species around binding energy 531.5 eV. Peak at 235.4 eV corresponds to O of adsorbed water (ref-Polyoxomolybdate anchored graphite oxide: Noble metal-free electrocatalyst for oxygen

reduction reaction. It is reported that a higher ratio of the concentration of surface adsorbed oxygen species ($O_{adsorbed}$) to oxygen present in the lattice($O_{lattice}$) would assist in the augmentation of catalytic activity (Arandiyan et al. 2013; Hou et al. 2013). Figure 5.7 (d) shows the high-resolution XPS spectrum confirms the existence of strontium. This spectrum has been deconvoluted in three peaks. The first among three is the characteristic peak of Sr $3d_{5/2}$ (lattice) at 133.0 eV, while the second broad peak at 135 eV is obtained by an overlap of Sr $3d_{5/2}$(surface) and Sr $3d_{3/2}$ (lattice). The third peak at 138 eV is characteristic of Sr $3d_{3/2}$(surface).

5.5 Magnetic studies

Figure 5.8 (a) illustrates the plot of measured magnetization versus applied magnetic field (M-H) curve at various selected temperatures for BSTO ceramic using Superconducting Quantum Design MPMS Magnetometer Interference Device (SQUID) observed from 5 K to 300 K at ±2 T. It is quite clear from the figure that magnetic nature is dominated by ferromagnetism at all the temperatures. The shift observed among the loops is attributed to spin flop, which relates to the disorderness generated in magnetic super lattices with the increasing temperature (García-Landa et al. 1999).

Variation of magnetization as a function of temperature at a constant applied field of 100 Oe was analyzed during the cooling process up to 5 K from room temperature (300 K). From figure 5.8 (b), The temperature dependences of ZFC and FC showed a sharp change of slope to a much faster decrease of magnetization in the range of 175 K. Thus, a sudden change in magnetic phase is observed. The origin of such variation in magnetization has been related to the large magnetocrystalline anisotropy (Singh et al. 2014).

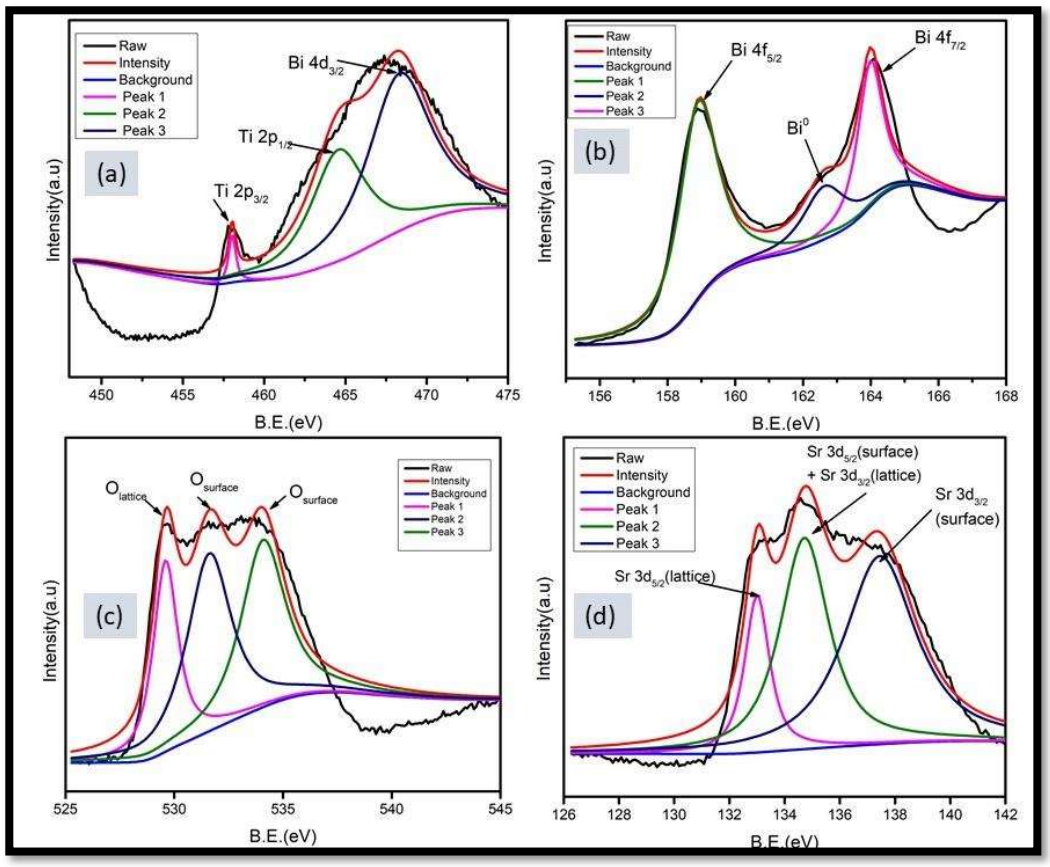

Figure 5.7 (a)–(d) High-resolution XPS spectra of the BSTO ceramics.

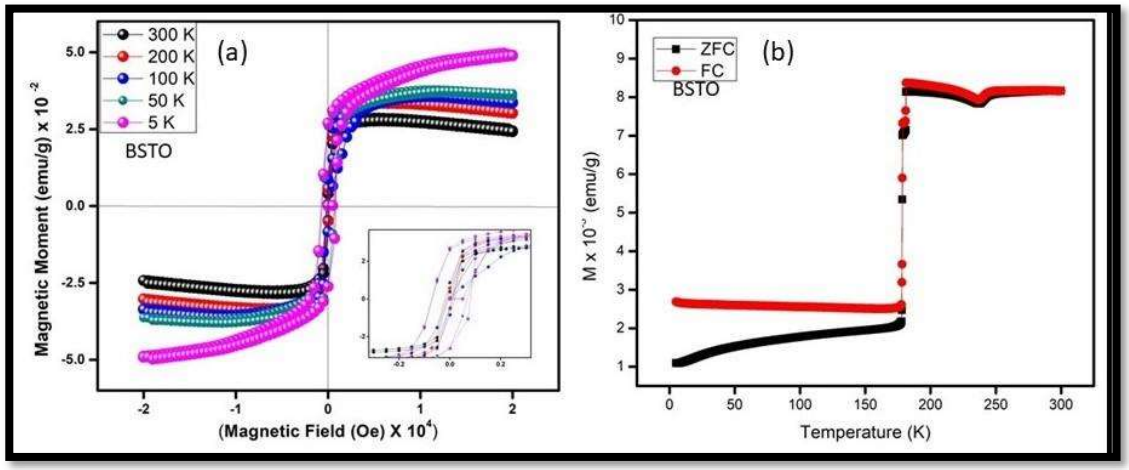

Figure 5.8 (a) M-H hysteresis loop from 5 K to 300 K and (b)Temperature-dependent ZFC and FC at H = 100 Oe for BSTO ceramic.

5.6 Impedance studies

Assessment of the electrical properties exhibited by the polycrystalline materials and understanding the role their microstructures natures in affecting them is effectively done by impedance analysis. Along with this, it also provides information on the co-occurrence of multi-polarization with their relaxation processes. The estimation of the participation of grains, grain boundaries and electrode interface to the overall capacitance and resistance can also be performed (Dumbrava and Svilainis). The complex impedance spectroscopy of the concerned BSTO ceramic can be seen in figure 5.9. However, instead of three, the only contribution of grain boundaries and electrode surface effects as only two semicircular arcs are witnessed in the figure. Inset of figure 5.9 shows data taken at a higher frequency, extrapolated on Z′ axis, the intercept of it is found to pass the Z′ axis ahead of origin.

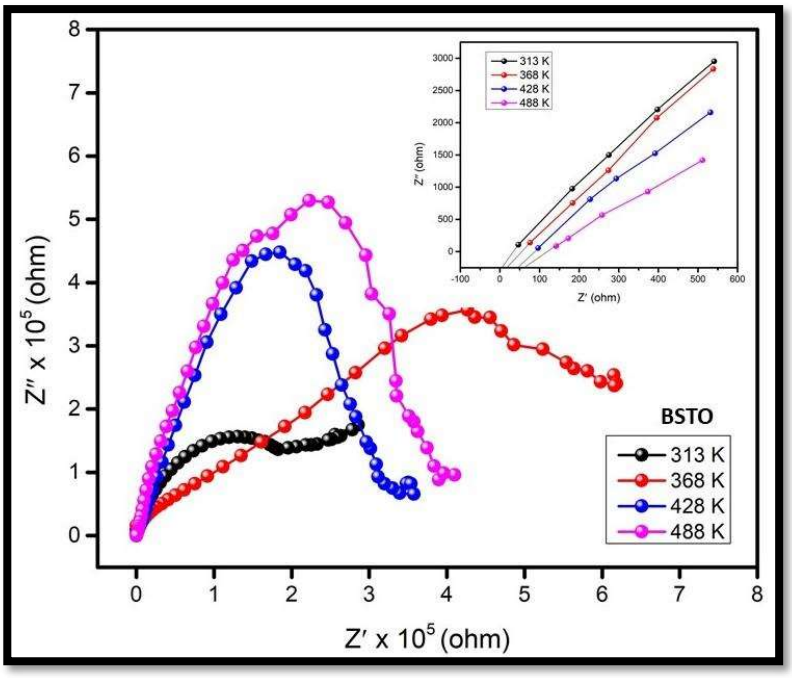

Figure 5.9 Complex impedence spectroscopy in a range of temperature (313 K-488 K) for BSTO ceramic and the inset is exhibiting an enlarged view of the higher frequencies.

Since the intercept doesn't pass through the origin, it can be said that another arc due to the contribution of grain is also present in higher frequency range, only it is beyond our measurement range. This intercept at Z' axis is regarded as the grains resistance (R_g). The grains capacitance (C_g), the resistance offered by grain boundaries (R_{gb}), and the capacitance of the grain boundary (C_{gb}) were evaluated and reported in table 5.3. The expression of impedance exerted by the grains and their boundaries is given by the following equation(Kumar et al. 2018).

$$Z^* = \frac{1}{R_g^{-1}+i\omega C_g} + \frac{1}{R_{gb}^{-1}+i\omega C_{gb}} = Z' - iZ'' \quad (5.2)$$

Where, $$Z' = \frac{R_g}{1+(\omega R_g C_g)^2} + \frac{R_{gb}}{1+(\omega R_{gb} C_{gb})^2} \quad (5.3)$$

And $$Z'' = R_g\left[\frac{\omega R_g C_g}{1+(\omega R_g C_g)^2}\right] + R_{gb}\left[\frac{\omega R_{gb} C_{gb}}{1+(\omega R_{gb} C_{gb})^2}\right] \quad (5.4)$$

where, R_g and R_{gb} are grain resistance and grain boundary resistance, respectively. C_g and C_{gb} are the grain capacitance and grain boundary capacitance, respectively; ω is the angular frequency. From the data calculated (as shown in table 5.3), it is witnessed that the contribution of grains for BSTO ceramic is less than that in case of grain boundaries, this validates the semiconducting behavior of grains having insulating boundaries, in accordance with the Inter-barrier layer capacitance (IBLC) mechanism.

The real and imaginary part of impedance varies as the function of temperatures, their variation at particular temperatures are shown in figure 5.10 (a) and figure 5.10 (b), respectively. The variation in both parts of impedance showcases similar behavior, the values of Z' and Z'' decrease with a rise in frequency, inferring an increment in ac conductivity (Thomas et al. 2017).

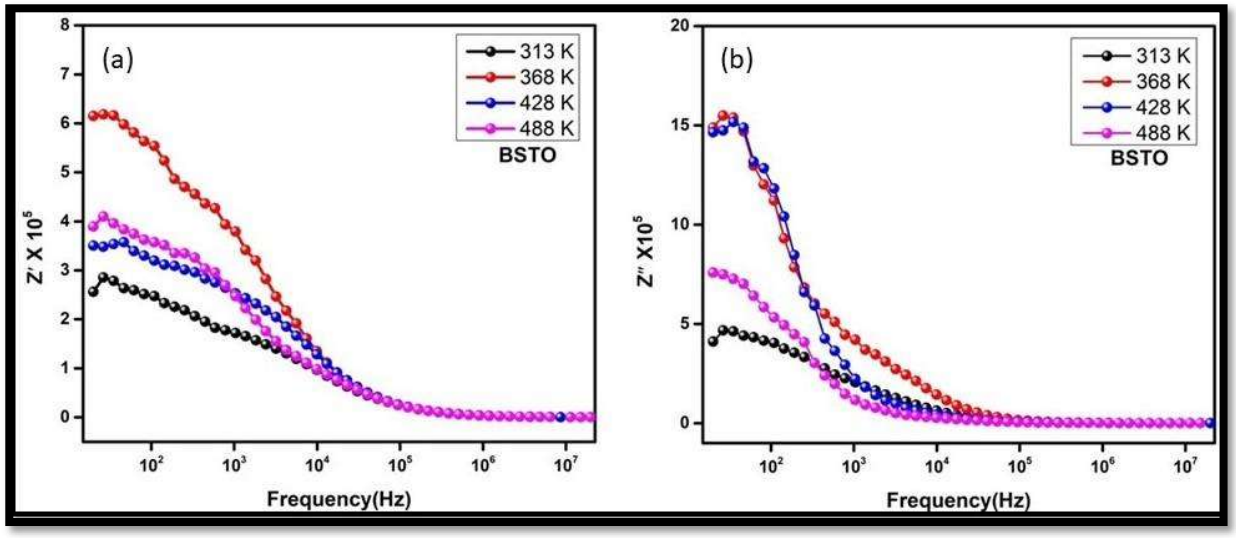

Figure 5.10 (a) variation of real part of impedance with temperature; (b) variation of imaginary part of impedance with temperature

Table 5.2 The resistance and capacitance exerted by grain boundaries and grains of BSTO ceramic at a few selected temperatures.

Temperature (K)	R_g (Ω)	C_g (pF)	R_{gb}(Ω) x 10^5	C_{gb} (pF)
313	146.53	0.543	5.13	0.416
368	455.96	0.175	18.35	0.632
428	263.27	0.302	46.5	1.48
488	238.72	0.334	63.14	6.42

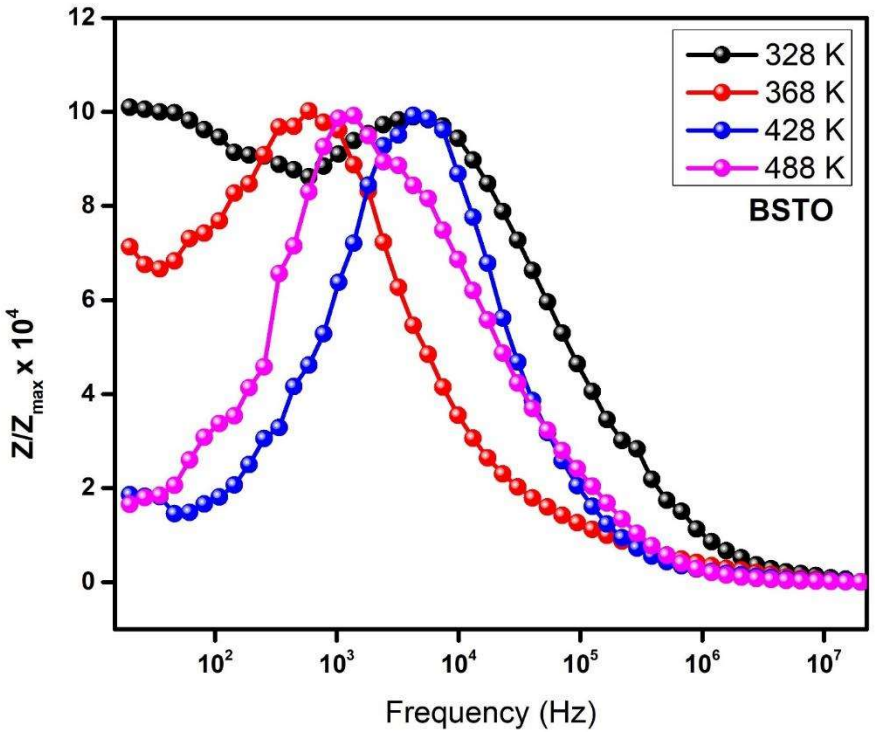

Figure 5.11 Normalized imaginary part of impedance as a function of frequency for BSTO ceramic.

The behavior of the normalized imaginary impedance part (Z″/Z″max) with the variation of frequencies at selected temperatures in BSTO ceramic can be seen in figure 5.11. at all the temperatures, single relaxation peaks are witnessed, but in the plot at 368 K in the lower frequency range, a short tail is also evident. The reason for the short tail can be attributed to the ample resistance exerted by electrode and grain boundary (Zhang et al. 2018). Another observation made is that single relaxation peaks shifts slightly in a higher frequency range with an increase in temperature, this deviation in peaks frequency is a result of the short-range motion of charge carriers suggesting the presence of thermally activated non-Debye like relaxation phenomena(Ke et al. 2010; Thomas et al. 2017). Peaks obtained in the lower frequency range highlight the contribution of grain boundaries, while in the higher frequency, it indicates more contribution of grains.

5.7 Dielectric Studies

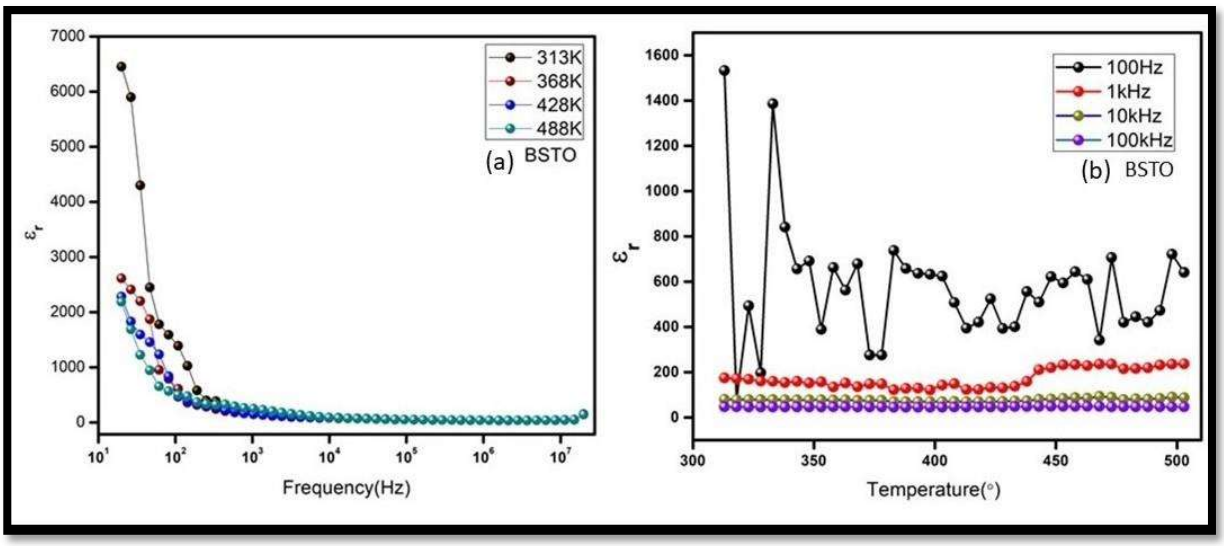

Figure 5.12 (a) Dielectric constant (ε_r) as a function of frequency; (b) Dielectric constant (ε_r) as a function of temperature for BBTO ceramic.

The effect of frequency on the dielectric constant for BSTO ceramic at four specific temperatures is portrayed in figure 5.12 (a). An increase in frequency causes the value of the dielectric constant to decrease, as can be seen in the figure. However, the fall in the values is steep in the lower frequency range because at the interface, accumulation of space charge occurs, which further causes the ionic medium to get polarized. In contrast, at a higher frequency range, a rapid switch in the field occurs, which makes it impossible for space charge to get accumulated at the interface leading to almost a constant value of the dielectric constant (Sharma et al. 2014). The value of dielectric constant at 368 K and 100Hz was found to be 2786 for BSTO ceramic.

The variation in the values of the dielectric constant with the temperature at few specific frequencies can be visualized in figure 5.12(b) for BSTO ceramic. Like other typical ferroelectric materials, BSTO ceramic also seems to reach maxima, and the corresponding temperature is

termed as Curie temperature, which indicates the phase change to paraelectric from the ferroelectric phase.

Figure 5.13 (a) portrays the influence of frequency on dielectric loss (tan δ) at four selected temperatures. The dielectric loss was observed to be decreasing with an increase in frequency. This inverse relationship was an outcome of energy dissipation due to the polarization that lags behind the frequency of the applied electric field (Yadava et al. 2017; Rani et al.). The presence of relaxation peaks is evident from the figure, arising due to the resonance of the frequency of the applied field with the hopping frequency of charge carriers (Delekar et al. 2012; Murugesan et al. 2015). The dielectric loss for BSTO ceramic at 100 Hz and 313 K is 4.3. Figure 5.13 (b) shows the variation of dielectric loss (tan δ) at four selected frequencies with the temperature. The plot gives the idea that the value of dielectric loss (tan δ) increases to attain maxima, then reduces swiftly. This behavior is in agreement with the Maxwell Wagner relaxation (Sharma et al. 2014).

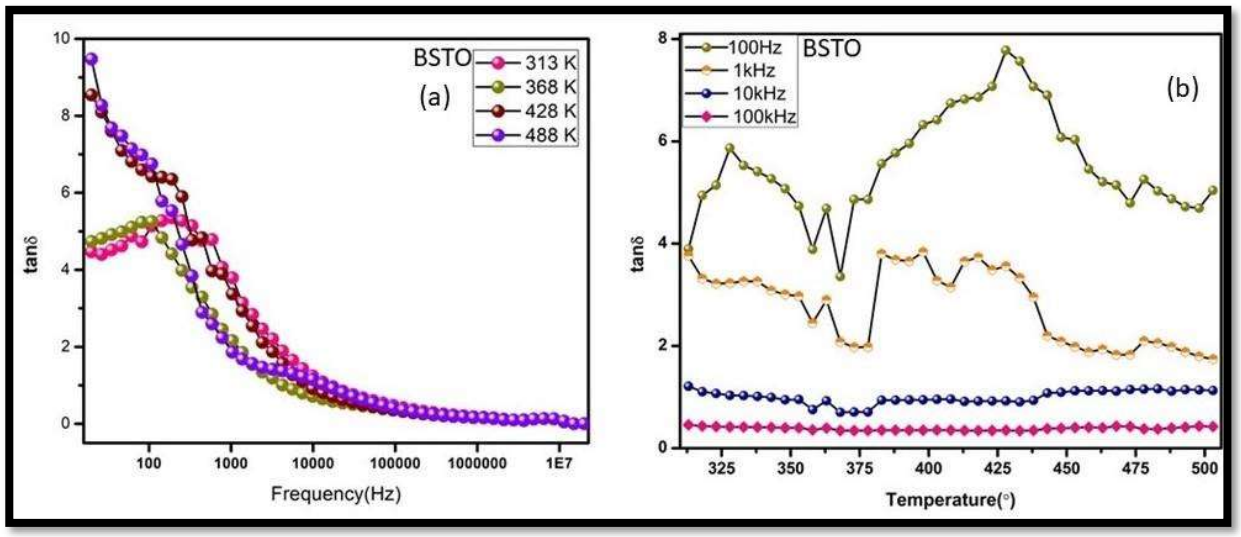

Figure 5.13 (a) Dielectric loss (tanδ) as a function of frequency; (b) Dielectric loss (tanδ) as a function of temperature for BBTO ceramic.

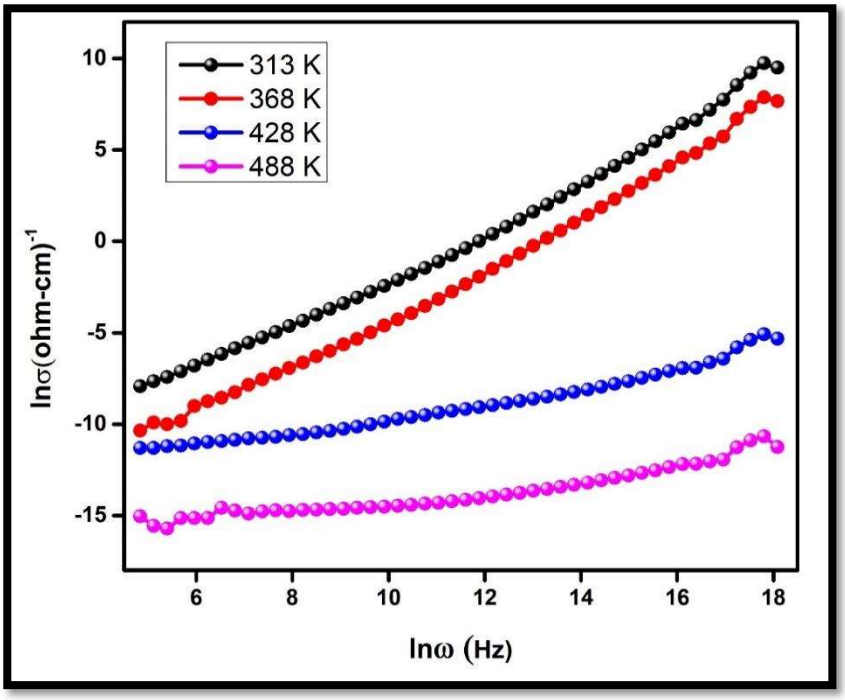

Figure 5.14 Frequency dependent AC conductivity at different temperatures for BSTO ceramic.

Figure 5.14 shows the activity of AC conductivity as a function of frequencies for the BSTO ceramic at four selected temperatures. It has already been established that for both states of solids, either disordered or ordered, the behavior of frequency driven ac conductivity resembles. The reason for the similarity in behavior is a consequence of the mode of conduction, that is, hopping charge carrier conduction, this mode is less favorable at a lower frequency range. Thus, in the lower range of frequency, AC conductivity is more temperature driven, while at a higher frequency range, frequency plays a major role (Shehata and Abdelhady 2018). The motion of charge carriers in hopping charge carrier conduction is considered to have discontinuous jumps, i.e., "hopping" among the well-defined localized sites present in the solids. The plot in figure 5.14 reveals that conductivity increases monotonically with frequency, which fits properly with "Joscher's universal power law" given in the equation below.

$$\sigma_{ac} \propto \omega^{n} \quad (5.5)$$

Where, n denotes the power-law exponent, within 0 < n < 1 value range. The power-law exponent values evaluated by fitting the plots in figure 5.14 are reported in table 5.4.

Table 5.3 The value of power-law exponent found for BSTO ceramic from the plots shown in figure 5.14 at a few selected temperatures.

Temperature	313 K	368 K	428 K	488 K
BSTO ceramic	0.31	0.44	0.87	0.93

These evaluated values eliminate the possibility of Debye-type relaxation, as for this relaxation, the value of the power-law exponent must be approximately 2. Thus, it confirms the existence of the Maxwell-Wagner relaxation process, also the thin oxide layering on the electrode induces the relaxation phenomena (Jonscher 1972).

5.8 Bandgap Analysis

For the analysis of optical properties and efficiency of the material, bandgap determination is necessary for clarifying the mechanism involved in photocatalysis and resolving which wavelength band of solar radiation will be appropriate for the procedures. The band gap of BSTO was evaluated by plotting the Tauc's plot using the data obtained from UV-DRS utilizing the following relation.

$$(\boldsymbol{\alpha h\nu})^{1/n} = \left(\boldsymbol{h\nu - E_g}\right) \quad (5.6)$$

where, α is the molar absorption coefficient, Eg is the optical band gap. Since it is the case of direct transition, thus the value of the exponent n is 1/2 (Viezbicke et al. 2015). Figure 5.15 unravels the optical band gap (Eg) to be as 3.14 eV, which is attained by extrapolating the linear fit of the plot

to intercept on the x-axis(hν) at a point, which corresponds to the band gap (Burnside et al. 1999). This value of the bandgap suggests that UV radiation is needed for photocatalysis.

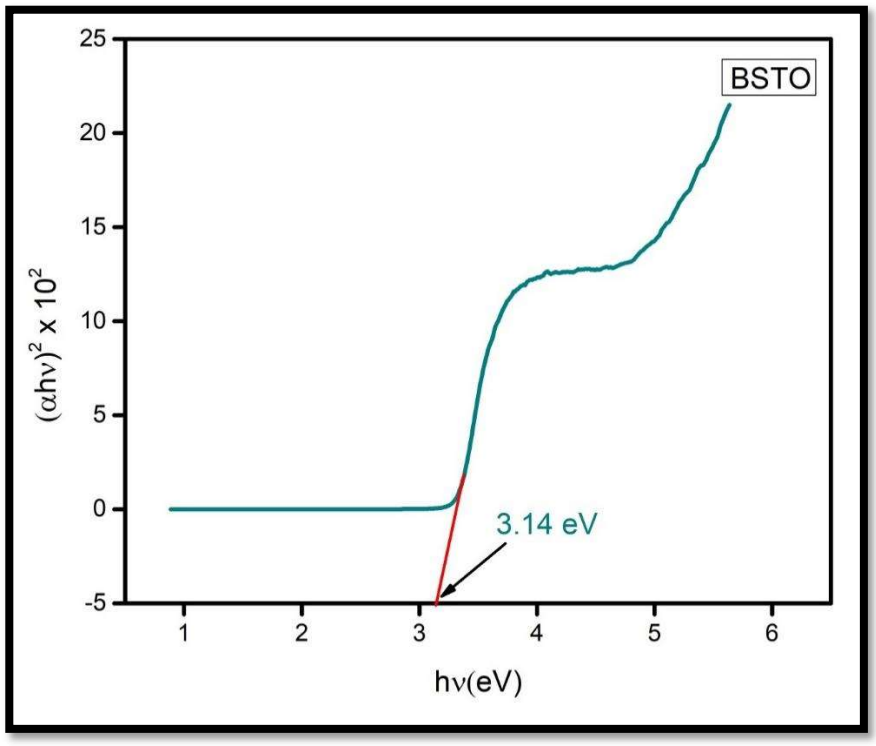

Figure 5.15 Tauc's Plot for BSTO ceramics.

5.9 BET Surface Area Analysis

For the analysis of BET specific surface area of BSTO, along with the information regarding its pore size distribution, we employed the nitrogen adsorption-desorption isotherms. The isotherm exhibited by BSTO is a distorted hysteresis loop at a relative pressure (P/P_o) close to unity as can be seen in figure 5.16, revealing the existence of a microporous structure, which can be categorized as type III according to IUPAC classification with characteristic H3-shaped hysteresis loops corresponds with pellets-like grains forming slit-like pores (Qi et al. 2017). The presence of pellets-like grains is also evident from the SEM images. The specific surface area of BSTO ceramic obtained with the analysis is 1.257 m^2g^{-1}.

The inset of the figure displays the BJH pore size distribution curves derived from the desorption branch. The BJH pore size distribution displays a wide range encompassing micropores, mesopores as well as macropores. However predominance in the range of 2~50 nm is evident, indicating mainly pores are mesoporous as pore-diameter within 1–100 nm limits are mesopores (Universiti Kebangsaan Malaysia et al. 2017). This range of Pore-diameter is enough to engulf the adsorbate molecules facilitating the phenomena of capillary condensation, thus boosting the catalytic activity (Kim and Ehrman 2009; Hall et al. 2012).

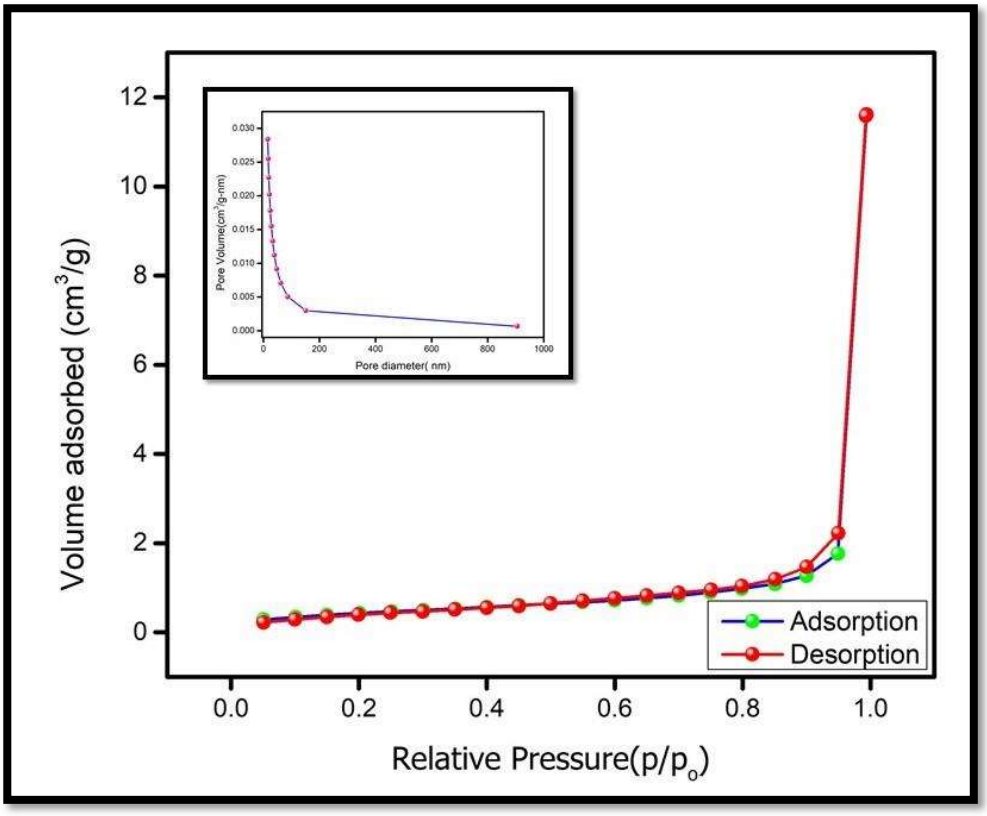

Figure 5.16 N_2 adsorption-desorption isotherms and the inset corresponding to pore-size distribution curves for BSTO ceramic.

5.10 Photocatalytic Efficiency

The photocatalytic activity of BSTO was assessed by degradation of Rhodamine B (RhB) dye, a common organic water pollutant, using solar light irradiation. Figure 5.17 (a) illustrates the Ultraviolet-Visible (UV-Vis.) Absorbance spectra for the RhB dye degradation in the presence of sunlight and absence of BSTO in 60 minutes, no considerable degradation took place.

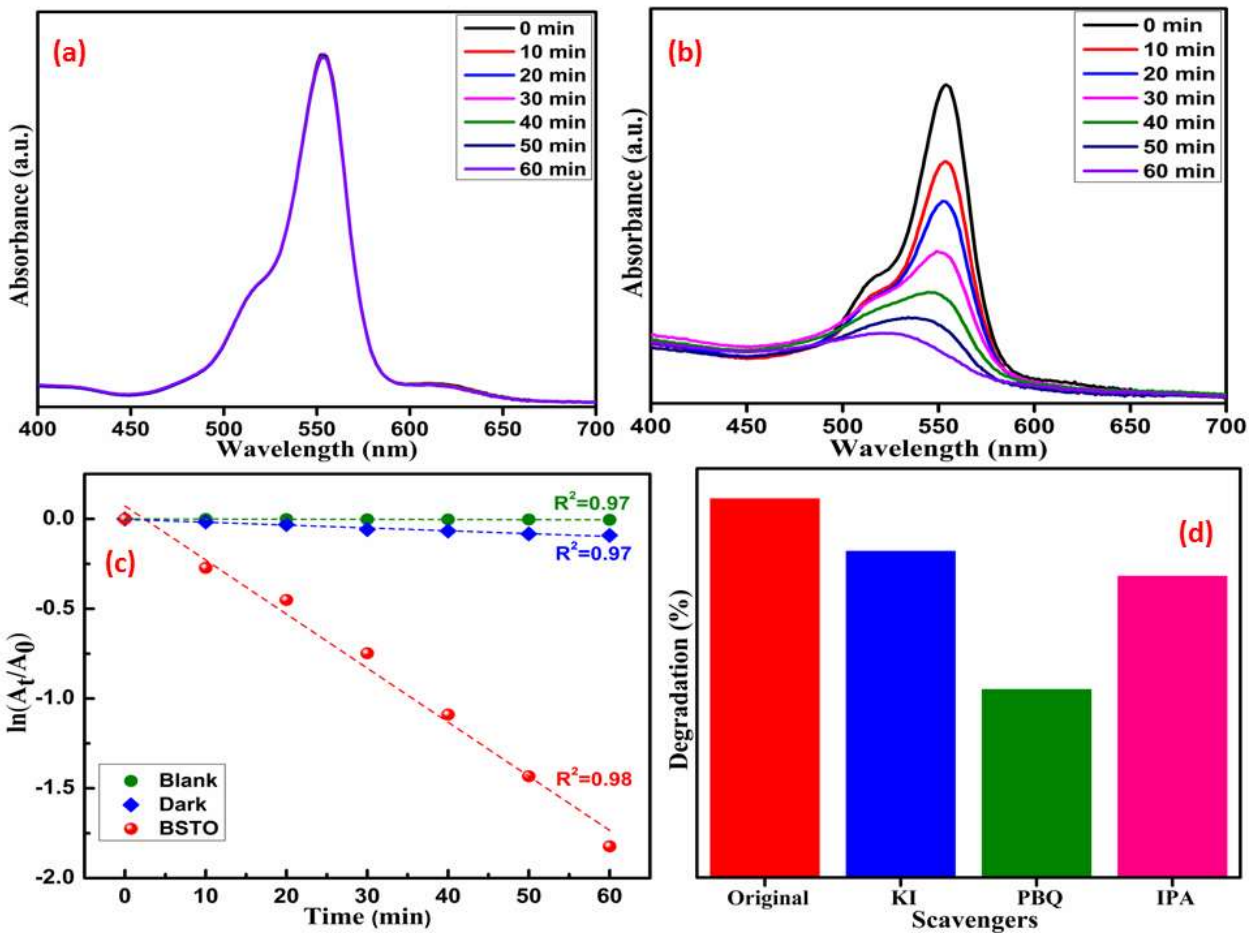

Figure 5.17 (a) UV-Vis absorbance spectra of BSTO photocatalyst, (b) UV-Vis absorbance spectra of RhB degradation by BSTO photocatalyst, (c) Kinetic first-order kinetic plot for RhB degradation by BSTO, (d) percentage degradation of RhB with different scavengers.

However, in figure 5.17 (b), it can be seen that it degraded almost 84% in 60 minutes in the presence of the material. The kinetic plot of $\ln(A_t/A_0)$ against irradiation time for RhB dye

degradation is displayed in figure 5.17 (c). The experimental data of the plot was found to fit well with the kinetics of first-order and K_{app} was calculated to be 3.0×10^{-3} while correlation coefficient (R^2) was found to be 0.98 for RhB dye degradation

In the photocatalytic experiment, various active species like superoxide radical ($O_2^{\cdot-}$), hydroxyl radical ($OH^{\cdot-}$), and holes (h^+) contribute a major role in the degradation of many organic recalcitrant. The scavengers like p-benzoquinone (PBQ), isopropyl alcohol (IPA), and potassium iodide (KI) were used to trap $O_2^{\cdot-}$ radicals, $OH^{\cdot}$ radicals, and holes (h^+) respectively formed during the degradation experiment. Figure 5.17 (c) displays the result of scavenging experiments for BTO-BT. The graph shows that RhB degradation was greatly inhibited by IPA than other trapping agents. IPA also has a negative effect on the photodegradation of RhB, while the addition of KI displays a minimum negative effect on the degradation of RhB. The above results show that $OH^{\cdot}$ radicals and $O_2^{\cdot-}$ are the major reactive species generated during the photocatalytic reaction. The order of active species generated during the catalytic experiment is $OH^{\cdot} > O_2^{\cdot-} > h^+$.

The recyclability test shown in figure 5.18 was performed to test the stability of the material as a photocatalyst and its degradation efficiency. The result obtained can be seen in the table shown in the figure, it can be observed that only approximately 6% decrement is observed after three cycles confirming the stability and high efficiency of the material (Wang et al. 2021).

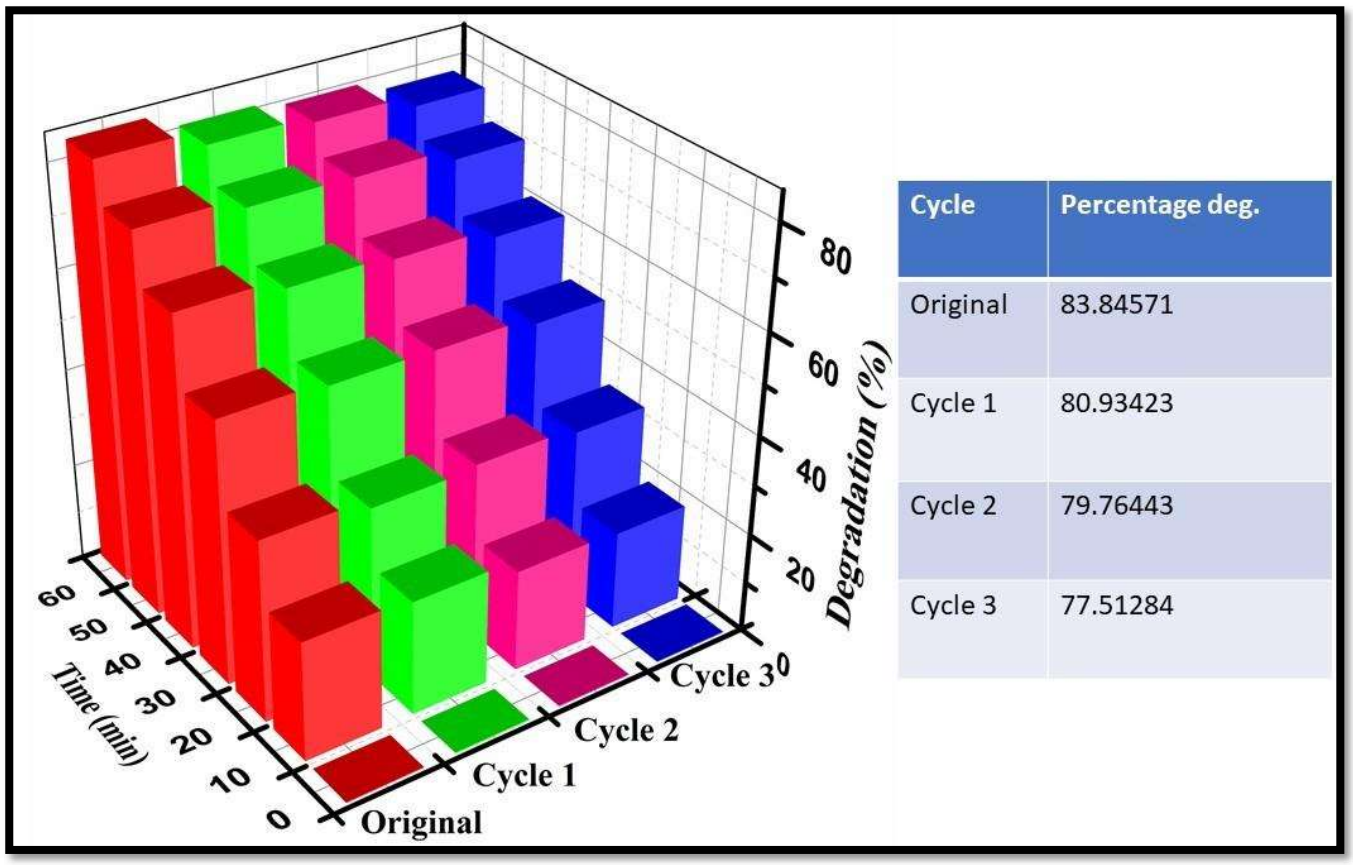

Cycle	Percentage deg.
Original	83.84571
Cycle 1	80.93423
Cycle 2	79.76443
Cycle 3	77.51284

Figure 5.18 Recyclability test of BSTO photocatalyst.

5.11 References

Arandiyan H, Dai H, Deng J, Liu Y, Bai B, Wang Y, Li X, Xie S, Li J. 2013. Three-dimensionally ordered macroporous La0.6Sr0.4MnO3 with high surface areas: Active catalysts for the combustion of methane. Journal of Catalysis. 307:327–339. doi:10.1016/j.jcat.2013.07.013.

Bantawal H, Krishna Bhat D. 2018. Hierarchical Porous Batio3 Nano-Hexagons as A Visible Light Photocatalyst. IJET. 7(4.5):105. doi:10.14419/ijet.v7i4.5.20022.

Benedek NA, Rondinelli JM, Djani H, Ghosez P, Lightfoot P. 2015. Understanding ferroelectricity in layered perovskites: new ideas and insights from theory and experiments. Dalton Trans. 44(23):10543–10558. doi:10.1039/C5DT00010F.

Chu M-W, Ganne M, Caldes MT, Brohan L. 2002. X-ray photoelectron spectroscopy and high resolution electron microscopy studies of Aurivillius compounds: Bi 4- x La x Ti 3 O 12 (x= 0, 0.5, 0.75, 1.0, 1.5, and 2.0). Journal of applied physics. 91(5):3178–3187.

Delekar SD, Yadav HM, Achary SN, Meena SS, Pawar SH. 2012. Structural refinement and photocatalytic activity of Fe-doped anatase TiO 2 nanoparticles. Applied Surface Science. 263:536–545. doi:10.1016/j.apsusc.2012.09.102.

Drits V. 1997. XRD Measurement of Mean Crystallite Thickness of Illite and Illite/Smectite: Reappraisal of the Kubler Index and the Scherrer Equation. Clays and Clay Minerals. 45(3):461–475. doi:10.1346/CCMN.1997.0450315.

Dumbrava V, Svilainis L. The Automated Complex Impedance Measurement System. :4.

Feng S, Huang G. 2001. Effects of emulsifiers on the controlled release of paclitaxel (Taxol®) from nanospheres of biodegradable polymers. Journal of Controlled Release.:17.

Galasso FS, Kestigan M. 2007. Bismuth Titanate, $Bi_4Ti_3O_{12}$. In: Murphy DW, Interrante LV, editors. Inorganic Syntheses. Hoboken, NJ, USA: John Wiley & Sons, Inc. p. 112–113. [accessed 2021 Jan 10]. http://doi.wiley.com/10.1002/9780470132616.ch24.

García-Landa B, Ritter C, Ibarra MR, Blasco J, Algarabel PA, Mahendiran R, García J. 1999. Magnetic and magnetotransport properties of the ordered perovskite Sr2FeMoO6. Solid State Communications. 110(8):435–438. doi:10.1016/S0038-1098(99)00079-4.

Giannuzzi LA, Stevie FA. 1999. A review of focused ion beam milling techniques for TEM specimen preparation. Micron. 30(3):197–204. doi:10.1016/S0968-4328(99)00005-0.

Hall MR, Tsang SCE, Casey SP, Khan MA, Yang H. 2012. Synthesis, characterization and hygrothermal behaviour of mesoporous silica high-performance desiccants for relative humidity buffering in closed environments. Acta Materialia. 60(1):89–101. doi:10.1016/j.actamat.2011.09.016.

Hervoches CH, Snedden A, Riggs R, Kilcoyne SH, Manuel P, Lightfoot P. 2002. Structural Behavior of the Four-Layer Aurivillius-Phase Ferroelectrics SrBi4Ti4O15 and Bi5Ti3FeO15. Journal of Solid State Chemistry. 164(2):280–291. doi:10.1006/jssc.2001.9473.

Hoo CM, Starostin N, West P, Mecartney ML. 2008. A comparison of atomic force microscopy (AFM) and dynamic light scattering (DLS) methods to characterize nanoparticle size distributions. J Nanopart Res. 10(S1):89–96. doi:10.1007/s11051-008-9435-7.

Hou D, Luo W, Huang Y, Yu JC, Hu X. 2013. Synthesis of porous Bi4Ti3O12 nanofibers by electrospinning and their enhanced visible-light-driven photocatalytic properties. Nanoscale. 5(5):2028. doi:10.1039/c2nr33750a.

Hou J, Cao R, Wang Z, Jiao S, Zhu H. 2011. Chromium-doped bismuth titanate nanosheets as enhanced visible-light photocatalysts with a high percentage of reactive {110} facets. J Mater Chem. 21(20):7296. doi:10.1039/c0jm04374e.

Jonscher AK. 1972. Department of Physics, Chelsea College, Pulton Place, London S.W.6, England. Journal of Non-Crystalline Solids. 10:293–315.

Ke Q, Lou X, Wang Y, Wang J. 2010. thin films. :1–7. doi:10.1103/PhysRevB.82.024102.

Kim S, Ehrman SH. 2009. Photocatalytic activity of a surface-modified anatase and rutile titania nanoparticle mixture. Journal of Colloid and Interface Science. 338(1):304–307. doi:10.1016/j.jcis.2009.06.047.

Kumar A, Yadava SS, Gautam P, Khare A, Mandal KD. 2018. Magnetic and dielectric studies of barium hexaferrite (BaFe12O19) ceramic synthesized by chemical route. Journal of Electroceramics.:1–10. doi:10.1007/s10832-018-0146-x.

Li X, Sun Y, Xiong T, Jiang G, Zhang Y, Wu Z, Dong F. 2017. Activation of amorphous bismuth oxide via plasmonic Bi metal for efficient visible-light photocatalysis. Journal of Catalysis. 352:102–112. doi:10.1016/j.jcat.2017.04.025.

Liang Y, Wang S, Guo P. 2017. Effects of Ag on the photocatalytic activity of multiple layer TiO_2 films. Materials Technology. 32(1):46–51. doi:10.1080/10667857.2015.1116821.

Liu G, Wang L, Yang HG, Cheng H-M, (Max) Lu GQ. 2010. Titania-based photocatalysts—crystal growth, doping and heterostructuring. J Mater Chem. 20(5):831–843. doi:10.1039/B909930A.

Liu Y, Zhang M, Li L, Zhang X. 2014. One-dimensional visible-light-driven bifunctional photocatalysts based on Bi4Ti3O12 nanofiber frameworks and Bi2XO6 (X=Mo, W) nanosheets. Applied Catalysis B: Environmental. 160–161:757–766. doi:10.1016/j.apcatb.2014.06.023.

Misra RDK, Girase B, Depan D, Shah JS. 2012. Hybrid Nanoscale Architecture for Enhancement of Antimicrobial Activity: Immobilization of Silver Nanoparticles on Thiol-Functionalized

Polymer Crystallized on Carbon Nanotubes. Adv Eng Mater. 14(4):B93–B100. doi:10.1002/adem.201180081.

Mohammed A, Abdullah A. SCANNING ELECTRON MICROSCOPY (SEM): A REVIEW. :9.

Murugesan C, Sathyamoorthy B, Chandrasekaran G. 2015. Structural, dielectric and magnetic properties of Gd substituted manganese ferrite nanoparticles. Physica Scripta. 90(8). doi:10.1088/0031-8949/90/8/085809.

Qi L, Tang X, Wang Z, Peng X. 2017. Pore characterization of different types of coal from coal and gas outburst disaster sites using low temperature nitrogen adsorption approach. International Journal of Mining Science and Technology. 27(2):371–377. doi:10.1016/j.ijmst.2017.01.005.

Rana S, Rawat J, Sorensson MM, Misra RDK. 2006. Antimicrobial function of Nd3+-doped anatase titania-coated nickel ferrite composite nanoparticles: A biomaterial system. Acta Biomaterialia. 2(4):421–432. doi:10.1016/j.actbio.2006.03.005.

Rani R, Kumar G, Batoo KM, Singh M. Electric and Dielectric Study of Zinc Substituted Cobalt Nanoferrites Prepared by Solution Combustion Method. American Journal of Nanomaterials.:4.

Shang M, Wang W, Ren J, Sun S, Zhang L. 2011. Nanoscale Kirkendall effect for the synthesis of Bi2MoO6 boxes via a facile solution-phase method. Nanoscale. 3(4):1474–1476. doi:10.1039/C0NR00974A.

Sharma S, Yadav SS, Singh MM, Mandal KD. 2014. Impedance spectroscopic and dielectric properties of nanosized Y 2/3 Cu 3 Ti 4 O 12 ceramic . Journal of Advanced Dielectrics. 04(04):1450030. doi:10.1142/s2010135x14500301.

Shehata MM, Abdelhady K. 2018. Temperature and frequency dependence of dielectric relaxation and AC electrical conductivity in p-Si/CuPc hybrid photodiode. Appl Phys A. 124(9):591. doi:10.1007/s00339-018-2006-6.

Shukla Y, Srivastava, Bhatnagar, Singh, Mishra, Kumar, Gupta. 2013 Apr. Synthesis of PLGA nanoparticles of tea polyphenols and their strong in vivo protective effect against chemically induced DNA damage. IJN.:1451. doi:10.2147/IJN.S26364.

Singh DK, Ganesan V, Yadav DK, Yadav M. 2020. Metal (Mn, Fe, Co, Ni, Cu, and Zn) Phthalocyanine-Immobilized Mesoporous Carbon Nitride Materials as Durable Electrode Modifiers for the Oxygen Reduction Reaction. Langmuir. 36(41):12202–12212. doi:10.1021/acs.langmuir.0c01822.

Singh S, Esakki Muthu S, Senyshyn A, Rajput P, Suard E, Arumugam S, Barman SR. 2014. Inverse magnetocaloric effect in Mn_2NiGa and $Mn_{1.75}Ni_{1.25}Ga$ magnetic shape memory alloys. Appl Phys Lett. 104(5):051905. doi:10.1063/1.4863742.

Sun D, Jin X, Liu H, Zhu J, Zhu Yudan, Zhu Yinyin. 2007. Investigation on FTIR spectrum of barium titanate ceramics doped with alkali ions. Ferroelectrics. 355(1 PART 1):145–148. doi:10.1080/00150190701517630.

Sunkara BK, Misra RDK. 2008. Enhanced antibactericidal function of W4+-doped titania-coated nickel ferrite composite nanoparticles: A biomaterial system. Acta Biomaterialia. 4(2):273–283. doi:10.1016/j.actbio.2007.07.002.

Thomas AK, Abraham K, Thomas J, Saban K V. 2017. Electrical and dielectric behaviour of Na 0.5 La 0.25 Sm 0.25 Cu 3 Ti 4 O 12 ceramics investigated by impedance and modulus spectroscopy. Journal of Asian Ceramic Societies. 5(1):56–61. doi:10.1016/j.jascer.2017.01.002.

Universiti Kebangsaan Malaysia, A. Ghani N 'Izzati, Mt Yusuf NY, Universiti Kebangsaan Malaysia, Wan Isahak WNR, Universiti Kebangsaan Malaysia, Masdar MS, Universiti Kebangsaan Malaysia. 2017. Modification of Activated Carbon from Biomass Nypa and Amine Functional Groups as Carbon Dioxide Adsorbent. JPS. 28(Suppl. 1):227–240. doi:10.21315/jps2017.28.s1.15.

Venkatasubramanian R, Srivastava RS, Misra RDK. 2008. Comparative study of antimicrobial and photocatalytic activity in titania encapsulated composite nanoparticles with different dopants. Materials Science and Technology. 24(5):589–595. doi:10.1179/174328408X282065.

Viezbicke BD, Patel S, Davis BE, Birnie DP. 2015. Evaluation of the Tauc method for optical absorption edge determination: ZnO thin films as a model system: Tauc method for optical absorption edge determination. Phys Status Solidi B. 252(8):1700–1710. doi:10.1002/pssb.201552007.

Wang W, Yang R, Li T, Komarneni S, Liu B. 2021. Advances in recyclable and superior photocatalytic fibers: Material, construction, application and future perspective. Composites Part B: Engineering. 205:108512. doi:10.1016/j.compositesb.2020.108512.

Yadava SS, Khare A, Gautam P, Kumar A, Mandal KD. 2017. Dielectric, ferroelectric and magnetic study of iron doped hexagonal Ba $_4$ YMn $_3$ O $_{11.5-\delta}$ (BYMO) and its dependence on temperature as well as frequency. New J Chem. 41(11):4611–4617. doi:10.1039/C6NJ04071C.

Zhang L, Wang H, Chen Z, Wong PK, Liu J. 2011 May. Bi2WO6 micro/nanostructures: Synthesis, modifications and visible-light-driven photocatalytic applications. Applied Catalysis B: Environmental.:S0926337311002098. doi:10.1016/j.apcatb.2011.05.008.

Zhang X, Wang X, Wang Q, Ma X, Liu Chunming, Li P, Liu Cailong, Han Y, Ma Y, Gao C. 2018. Hydride ion (H -) transport behavior in barium hydride under high pressure. Physical Chemistry Chemical Physics. 20(13):8917–8923. doi:10.1039/c7cp08386f.

Zhao X, Yang H, Cui Z, Wang X, Yi Z. 2019. Growth Process and CQDs-modified Bi4Ti3O12 Square Plates with Enhanced Photocatalytic Performance. Micromachines. 10(1):66. doi:10.3390/mi10010066.